Materials Advances

ROYAL SOCIETY OF CHEMISTRY

PAPER

View Article Online
View Journal | View Issue

Cite this: *Mater. Adv.*, 2024, 5, 2368

Top-down surfactant-free electrosynthesis of magnéli phase Ti_9O_{17} nanowires†

Peter M. Schneider, ‡[a] Christian M. Schott,‡[a] Dominik Maier,[a] Sebastian A. Watzele,[a] Jan Michalička,[b] Jhonatan Rodriguez-Pereira,[bc] Ludek Hromadko,[c] Jan M. Macak,*[bc] Volodymyr Baran,[d] Anatoliy Senyshyn,[e] Arnaud Viola,[fg] Frédéric Maillard,[fg] Elena L. Gubanova*[a] and Aliaksandr S. Bandarenka*[ah]

TiO_2 nanowires have proven their importance as a versatile material in numerous fields of technology due to their unique properties attributable to their high aspect ratio and large surface area. However, synthesis is an enormous challenge since state-of-the-art techniques rely on complex, multi-stage procedures with expensive, specialized equipment, employing high-temperature steps and potentially toxic precursor materials and surfactants. Hence, we elucidate a simple and facile top-down methodology for the synthesis of nanowires with non-stoichiometric Magnéli phase Ti_9O_{17}. This methodology relies on the electrochemical erosion of bulk Ti wires immersed in an aqueous electrolyte, circumventing the use of environmentally harmful precursors or surfactants, eliminating the need for high temperatures, and reducing synthesis complexity and time. Using multiple techniques, including transmission electron microscopy, X-ray photoelectron spectroscopy, and X-ray diffraction, we provide evidence of the successful synthesis of ultrathin nanowires with the crystal structure of non-stoichiometric Ti_9O_{17} Magnéli phase. The nanowire width of ~5 nm and the Brunauer–Emmett–Teller surface area of ~215 $m^2\ g^{-1}$ make the nanowires presented in this work comparable to those synthesized by state-of-the-art bottom-up techniques.

Received 5th November 2023,
Accepted 26th January 2024

DOI: 10.1039/d3ma00968h

rsc.li/materials-advances

Introduction

Titanium dioxide (TiO_2) is a widely used class of transition metal oxide materials with many different fields of application. These reach from energy storage systems, such as batteries[1] and supercapacitors,[2] over a variety of sensor systems,[3] to photocatalysis,[4] which has gained ever-growing research interest since Fujishima and Honda discovered photocatalytic water splitting on TiO_2 using ultraviolet light in 1972.[5] Besides photoelectrochemical water splitting, composites of CeO_2/TiO_2 showed remarkable photocatalytic activity for the degradation and mineralization of tetracycline at room temperature.[6] Furthermore, Ti-based materials have gathered increasing interest as micro- or nanoporous layers in electrolyzers for efficient hydrogen production due to their unique properties of minimizing interfacial resistance between the catalyst and gas diffusion layer.[7] Besides this, nanostructured TiO_2 holds great potential in other branches of heterogeneous catalysis, either directly as a catalyst[8] or, most importantly, as a catalyst support material.[9] For the former, Ni/TiO_2 catalyst systems, as an example, revealed high catalytic activity and stability for undiluted methane decomposition under high-temperature conditions.[10] The latter functions as a framework to which catalysts can attach. As a result, the catalyst support material can contribute to the total catalyst stability and activity by preventing agglomeration and maximizing the accessible number of the catalyst's active surface sites. Therefore, support materials must exhibit a large surface-to-volume ratio; hence nanostructured morphologies are indispensable.

[a] *Physics of Energy Conversion and Storage, Technical University of Munich, James-Franck-Str. 1, 85748 Garching, Germany. E-mail: elena.gubanova@tum.de, bandarenka@ph.tum.de*
[b] *Central European Institute of Technology, Brno University of Technology, Purkynova 123, 61200 Brno, Czech Republic. E-mail: Jan.Macak@ceitec.vutbr.cz*
[c] *Center of Materials and Nanotechnologies, University of Pardubice, Nam. Cs. Legii 565, 53002 Pardubice, Czech Republic*
[d] *Deutsches Elektronen Synchrotron (DESY), Notkestr. 85, 22607 Hamburg, Germany*
[e] *Heinz Maier-Leibnitz Zentrum (MLZ), Technische Universität München, Lichtenbergstr. 1, 85748, Garching, Germany*
[f] *Univ. Grenoble Alpes, Univ. Savoie Mont Blanc, CNRS, Grenoble INP, LEPMI, 38000 Grenoble, France*
[g] *Institute of Engineering and Management Univ., Grenoble Alpes, France*
[h] *Catalysis Research Center TUM, Ernst-Otto-Fischer-Str. 1, 85748 Garching, Germany*

† Electronic supplementary information (ESI) available. See DOI: https://doi.org/10.1039/d3ma00968h

‡ P. M. Schneider and C. M. Schott contributed equally to this work.

Various classes of support materials exist to date, of which mesoporous materials,[11] conductive polymers,[12] carbon-based materials,[13] and metal oxides[14] are the most important ones. Metal oxides, such as tungsten oxide (WO_3), cerium oxide (CeO_2), and TiO_2, offer significant advantages compared to the other support materials classes. Apart from excellent mechanical, thermal, and chemical stability, they profit from the strong metal–support interaction (SMSI), which stabilizes the active metal catalyst and improves the catalytic activity.[15] TiO_2 nanowires meet these requirements and thus belong to the state-of-the-art support materials in the class of metal oxides due to their excellent chemical stability under catalytic conditions, resistance to corrosion and oxidation, mechanical strength, and large surface area.[16] Moreover, Ti is one of the most abundant, non-toxic, and environmentally friendly materials, making TiO_2 nanowires an ideal candidate for a sustainable catalyst support material.[17] However, the toxicity of nanomaterials, such as nanoparticles or nanowires, has been shown in various studies and should be addressed.[18] Nevertheless, nanomaterials have become indispensable in modern technologies. Obeying standard health and safety protocols for handling nanomaterials allows the synthesis, handling, and application of novel nanomaterials, such as the Ti_9O_{17} nanowires presented in our study. Besides TiO_2, non-stoichiometric titanium oxides with the general formula Ti_xO_{2x-1} $(4 \leq x \leq 10)$ have been reported to show distinctive properties, such as great stability until almost 2000 K, and superior corrosion stability in acidic and alkaline environments.[19] Their unique structure, consisting of rutile layers separated by shear planes, leads to a high electronic conductivity compared to TiO_2.[20] Due to the superior properties of non-stoichiometric TiO_x, these so-called Magnéli phases are a promising class of materials for application in the field of electronics or energy systems, *i.e.*, as catalyst support material in (electro) catalysis, compared to classical TiO_2.[21] Magnéli-phase Ti_xO_{2x-1} revealed significant durability as a support material for palladium catalysts in alkaline direct ethanol fuel cells[22] and platinum catalysts in formic acid electrooxidation.[23] In addition, the Magnéli phase proved to be an excellent candidate for thermoelectric applications.[19,24]

However, the production of nanostructured titanium oxides (TiO_x) poses a severe challenge despite the diverse variety of synthesis methods available to date. The most common approaches include, among others, sol–gel, hydrothermal, solvothermal, microwave-assisted, surfactant-assisted, and sonochemical methods, as well as chemical and physical vapor deposition.[25] Nonetheless, the synthesis of TiO_2-like nanowires usually relies on complicated multi-step approaches at elevated temperatures or pressures utilizing additives, such as surfactants, which can be harmful to the environment. For example, in physical and chemical vapor deposition, Ti vapor condenses at the surface of a substrate and forms a solid-phase nanostructure. However, raw Ti first needs to be brought to its vapor phase requiring high temperatures in the range of 500–700 °C, making it an environmentally unfavorable technique. The sol–gel method is a common bottom-up approach to producing inorganic ceramic and glass materials but usually requires a mixture of precursor solutions with subsequent stirring, drying, and heating at high temperatures of up to several 100 °C for several hours to obtain the final TiO_x nanowires. As another standard bottom-up synthesis technique for TiO_x nanostructures, the hydrothermal method covers the heterogeneous reactions of Ti precursor mixtures in aqueous solutions.[16] Unfortunately, several synthesis steps at elevated temperatures and pressures, usually for several hours or days, are necessary to form the desired nanostructures. In contrast to hydrothermal, solvothermal approaches use organic solvents instead of aqueous ones. This utilization of organic solvents results in temperatures and pressures even higher than for the hydrothermal method, which enables better control of the TiO_x size and morphology. Still, it also requires more energy during the synthesis process.

The addition of surfactants demonstrates a standard procedure to control the growth of nanostructured TiO_x synthesized by the bottom-up approaches mentioned before.[26] However, the addition of surfactants during the synthesis constitutes several concerns. Primary and secondary toxicity, biodegradability, eco-friendliness, and environmental pollution remain immense problems.[27] In addition, surfactant residues at the surface of the nanomaterial after synthesis are detrimental to its performance as they can block the nanomaterial's surface and, therefore, impair its unique properties. Consequently, we present a novel, alternative, top-down approach to synthesizing Magnéli phase Ti_9O_{17} nanowires without needing elevated temperatures or using environmentally harmful substances, such as surfactants, called electrochemical erosion. Even though reported by Bredig and Haber as early as the end of the 19th century,[28] this approach only gained increasing interest in recent years as the groups of Li and Koper employed it to successfully fabricate various metal nanostructures including Bi, Pt, Rh, Au, Cu, Ag, Ni, and Si, among others.[29] In previous studies, our group explored the synthesis of platinum-lanthanide nanoparticles and the influence of the synthesis parameters on Pt nanoparticles.[30]

Experimental

Synthesis

To fabricate ultrathin non-stoichiometric Ti_9O_{17} nanowires with a high surface area, two Ti bulk wires (Ø 0.25 mm, 99.6%, MaTecK, Germany) were immersed in a saturated KOH solution (85%, Grüssing, Germany) and subjected to an alternating current (AC) signal to initiate electrochemical erosion using a VSP 300 potentiostat (Bio-Logic, France). The influence of the AC signal frequency and solution composition on the nanostructure size, morphology, and composition is further elucidated in the ESI.† Using a sinusoidal voltage signal with an amplitude of 25 V and a frequency of 200 Hz, we eroded the bulk Ti wires into ultrathin Ti_9O_{17} nanowires. The formation of Ti_9O_{17} nanowires occurred immediately during the synthesis process in the saturated KOH electrolyte through oxidation, indicated by a change in the color of the eroded Ti from dark grey (Ti) to white (Ti_9O_{17} nanowires). Subsequently,

the saturated KOH electrolyte containing the Ti_9O_{17} nanowires was diluted, filtered, washed with ultrapure water (18.2 MΩ cm, Merck Millipore, USA) and ethanol (EMSURE® ACS, ISO, Reag. Ph Eur, Sigma Aldrich®, USA), and dried in a furnace (Heraeus, Germany) at 60 °C in air to obtain Ti_9O_{17} nanowires. More detailed information on the synthesis procedure and materials can be found in the ESI.† Here, we highlight the simplicity of our approach, which can be carried out in one pot within one step with subsequent filtering, washing, and drying at low temperatures. No surfactants, precursor solution mixtures, complicated multi-stage synthesis protocols, or elevated temperatures are needed compared to other state-of-the-art approaches mentioned before.

Characterization methods

Adsorption measurements. Adsorption measurements with N_2 at −196.15 °C were carried out on a 3Flex Physisorption from Micromeritics Instrument Corp., which uses a manometric method to determine the amount adsorbed under equilibrated gas pressure. Adsorption data were processed using the 3Flex Software Version 5.01 by Micromeritics Instrument Corp. and plotted in OriginPro 2021b by OriginLab Corp. Samples were transferred into pre-weighed sample tubes and capped with Micromeritics CheckSeals. Samples were subsequently activated again at room temperature for 12 h under a dynamic vacuum of $\sim 10^{-3}$ mbar using a SmartVac Prep by Micromeritics Instrument Corp. to ensure the absence of unwanted adsorbates and identical pre-measurement states of all samples. The mass of the adsorbent was then recorded, generally in the range of 25–100 mg. A liquid nitrogen bath is used for the measurements at −196.15 °C. The surface area of the materials was derived using the Brunauer–Emmett–Teller (BET) model, hence given as the 'BET surface' and based on N_2-isotherms measured at −196.15 °C. To determine the apparent BET area – or more precisely: BET capacity – for microporous materials, care was taken to adhere to the Rouquerol criteria.

Transmission electron microscopy (TEM). The morphology, structure, and chemical composition of the TiO_x nanowire network was studied in nanoscale with a C_s image-corrected transmission electron microscope TITAN Themis 60–300 Cubed (Thermo Fisher Scientific, USA). The high-resolution imaging with sub-Angstrom resolution, selected area electron diffraction (SAED) acquisition, and scanning TEM- energy dispersive X-ray spectroscopy (STEM-EDX) elemental mapping was conducted with an acceleration voltage of 300 kV. STEM-electron energy loss spectroscopy (STEM-EELS) elemental mapping was conducted with 120 kV and an electron beam current of ∼100 pA to mitigate electron beam damage during the probing of single nanowires. Additional TEM images were taken using a JEOL 2010 microscope bearing a LaB_6 filament and operated at 200 kV (resolution 0.19 nm). EDX spectroscopy was performed with a Super-X detector and elemental maps and chemical composition measurements in atomic percentage (at%) were acquired and processed in the software Velox utilizing a standard Cliff–Lorimer (*K*-factor) quantification method. EELS was performed with Gatan GIF Quantum ERS spectrometer and EEL spectrum images and elemental maps were acquired and processed with the software GMS3 utilizing a model-based quantification.[31] A sample for TEM analysis was prepared from a dispersed solution made of TiO_x powder and pure ethanol, which was drop-casted onto a copper TEM grid coated with a carbon holey membrane.

X-Ray photoelectron spectroscopy (XPS). The surface chemical composition and electronic state of the TiO_x nanostructures were determined by XPS (ESCA2SR, Scienta-Omicron) using a monochromatic Al K_α (1486.7 eV) X-ray source operated at 250 W. The samples were fixed in the sample holders with carbon conductive adhesive tape. The measurements were carried out in the analysis chamber with a pressure of around 1×10^{-9} mbar. The surface charge compensation of the samples was controlled with a charge neutralizer (CN 10). The binding energy (BE) scale of the spectra was corrected taking the adventitious carbon at 284.8 eV as a reference. The data analysis was performed with the CasaXPS software (Casa software Ltd) using the elemental sensitivity factors provided by the manufacturer. For the fitting procedure, a Shirley baseline was used together with the Gaussian–Lorentzian function (70–30).

Structural studies. A series of structural studies applying synchrotron radiation were performed at ambient temperature using the beamline (P02.1) at PETRA III, DESY. Fixed photon energy of 60 keV (λ = 0.20723 Å) was used.[32] Diffraction patterns were collected using a VAREX area detector at two distinct sample-to-detector distances of 350 mm and 2200 mm, corresponding to the pair distribution function (PDF) and high-resolution diffraction (XRD) modes, accordingly. Exposure times for each diffraction pattern were 20 min and 1 min in PDF and XRD modes, respectively. Azimuthal data integration was carried out using pyFAI applying LaB_6 (NIST, SRM660c) as a reference.[33] Powder samples were contained in sealed glass capillaries with 0.7 mm diameter, where diffraction data collection was performed under constant capillary spinning. Analysis of obtained XRD patterns was performed by the full profile analysis\decomposition using FullProf program package.[34] To model the peak profile shape, the pseudo-Voigt function in Thompson–Cox–Hastings setting was chosen. Background contribution was determined using a linear interpolation between selected data points in non-overlapping regions and subtracted from the dataset. Total scattering data were reduced using PDFGetX3 software.[35] The accessible range of momentum transfer was Q = 31.8 Å^{-1}, whilst due to obtained signal-to-noise and instrumental geometry the meaningful $Q_{max\text{-}inst}$ and Q_{max} limits were set to 20 Å^{-1} and 16 Å^{-1}, accordingly.

Scanning electron microscopy (SEM). The morphology of the prepared samples was examined by SEM (JEOL JSM 7500F, Japan) with a field-emission cathode. The samples were observed without any conductive coating.

Results and discussion

Nanowire morphology and BET surface analysis

The ultrathin nanowires synthesized in saturated KOH are characterized *via* TEM in Fig. 1. The TEM images were used

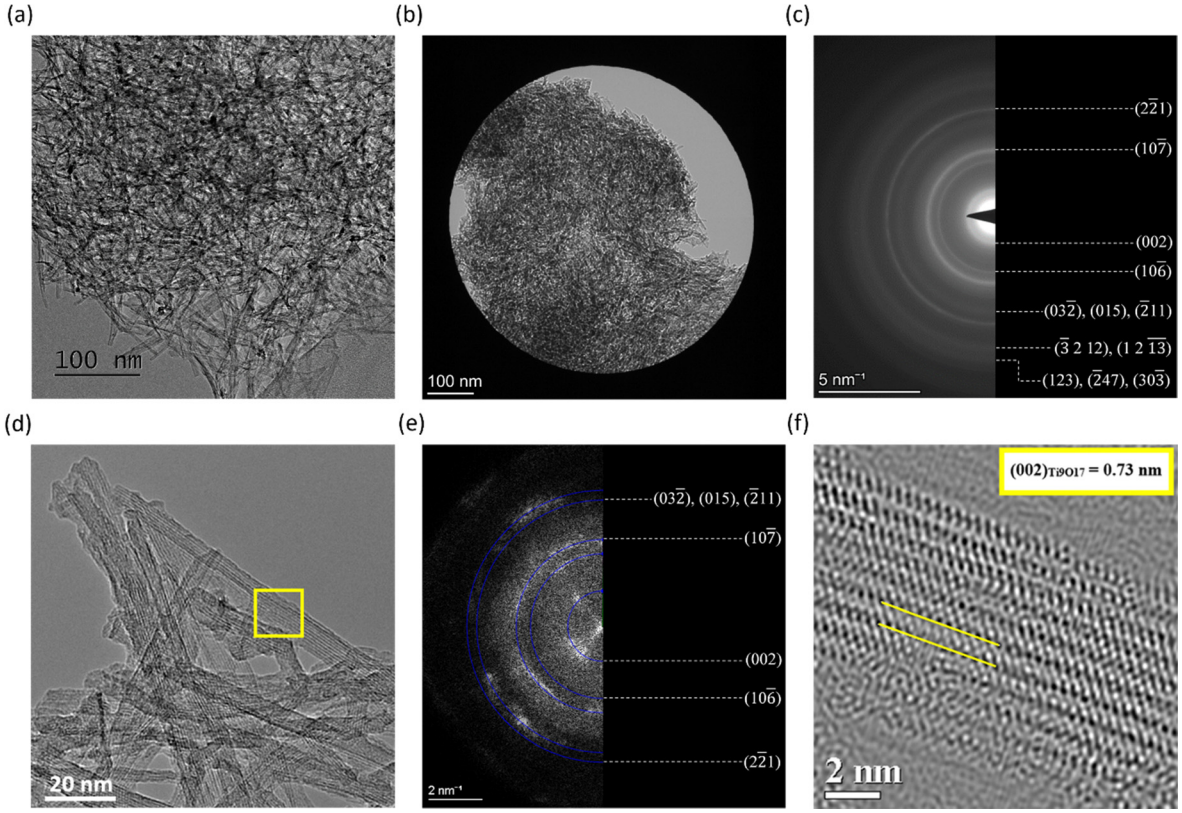

Fig. 1 A set of TEM characterizations of nanowires synthesized in saturated KOH. (a) Overview image of a nanowire network. (b) TEM image showing an encircled volume of a SAED aperture for diffraction analysis and (c) a resulting electron diffraction pattern with rings corresponding to lattice planes of the Ti_9O_{17} crystal phase. (d) HR-TEM image of a nanowire network with atomic resolution and (e) an FFT pattern of nanowires observed in HR-TEM revealing spots from lattice planes of the Ti_9O_{17} phase. (f) HR-TEM image showing in detail the atomic structure of a single nanowire marked in (d) and revealing the (002) lattice plane stacking with a *d*-spacing of 0.73 nm.

to estimate the width of the nanowires, which corresponded to approximately (5.0 ± 0.6) nm. Furthermore, the nanowires showed high isotropy, forming a complex nano-structural network. The length of the nanowires is estimated to be in the range of micrometers. We determined the surface area of the ultrathin nanowires to be (215 ± 15) $m^2\ g^{-1}$ from adsorption and desorption isotherms *via* BET measurements, as shown in Fig. 2. The isotherms resulting from the BET analysis of various other nanostructures synthesized with different parameters are illustrated in Fig. S2a and b (ESI†). The determined BET surface area competes with reported values for TiO_2 nanowires synthesized *via* more traditional methods, such as anodic oxidation, electrospinning, hydrothermal, and one-pot solvothermal, for which the BET surface areas correspond to (12–89) $m^2\ g^{-1}$, (68–95) $m^2\ g^{-1}$, (112–232) $m^2\ g^{-1}$, and 67.2 $m^2\ g^{-1}$, respectively.[36] Obtaining state-of-the-art BET surface areas with this simple and facile electrochemical erosion approach is advantageous, as it does not use environmentally harmful substances, like organic additives. Furthermore, the inset in Fig. 2 displays the pore size distribution of the nanowires revealing micropores in the sub-nanometer regime, indicated by the peak at ∼0.8 nm pore width. In addition, we observed bigger pores with sizes in the range of ∼3 nm to ∼40 nm. The rather continuous behavior of the pore size distribution in this region arises most likely due to the mesoporous character of the highly isotropic nano-structure network of the Ti_9O_{17} nanowires, contributing to the high BET surface area.

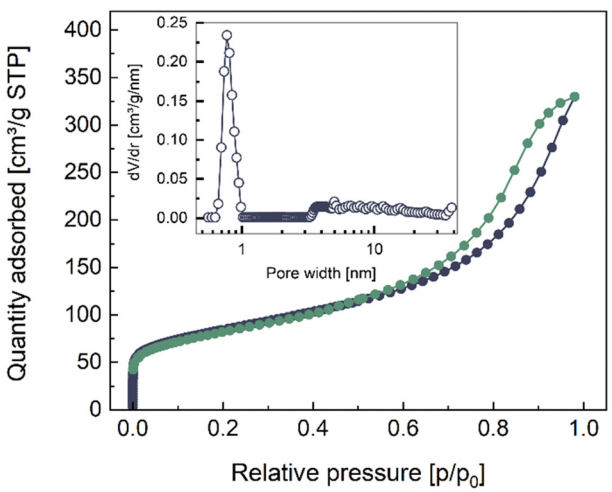

Fig. 2 N_2 adsorption (black) and desorption (green) isotherms of the Ti_9O_{17} nanowires synthesized in saturated KOH *via* electrochemical erosion. The inset shows the pore size distribution with a strong peak around ∼0.8 nm.

Structural TEM characterization of Ti_9O_{17} nanowires

A SAED analysis of a broader region containing a large number of nanowires, as shown in Fig. 1b and c, gives insights into the lattice structure of the nanowires. An evaluation of lattice spacings and ring intensities from the SAED pattern and a comparison of obtained results with crystallographic standards for Ti (hcp) and various TiO_x titanates indicated that the nanowires synthesized by electrochemical erosion have the structure of a non-stoichiometric Ti_9O_{17} with triclinic $P\bar{1}$ lattice, a so-called Magnéli phase of TiO_2.[37] The presence of any other crystal phases can be excluded based on the SAED analysis. The same results are confirmed by HR-TEM, and fast Fourier transformation (FFT) characterization of the nanorod network imaged with atomic resolution, shown in Fig. 1d and e, where FFT patterns also reveal *d*-spacings in good agreement with the Ti_9O_{17} lattice planes. In addition, HR-TEM imaging reveals the presence of crystal lattice plane stacking along the length of nanowires. This lattice stacking is characteristic of the synthesized nanowires, which is demonstrated in Fig. 1f at a detail of a nanowire marked by a yellow rectangle in Fig. 1d. The measured value of ~0.73 nm matches with (002) lattice planes of the Ti_9O_{17} crystal structure. Interestingly, minor differences in lattice plane *d*-spacings were revealed occasionally, for example, between the (002) planes when measurements of either SAED or FFT patterns showed a *d*-spacing of ~0.76 nm, which is slightly larger than the standard value. It suggests a presence of strain in the lattice, possibly resulting from the electrochemical synthesis of the nanowires.

In the following part, we discuss the results obtained by multiple techniques, including XPS, EDX, high-resolution XRD (HR-XRD), PDF, and EELS to confirm the findings made by the HR-TEM imaging with SAED and FFT characterization.

XPS examination of Ti_9O_{17} nanowires

The XPS results, depicted in Fig. 3a and b, display the $2p_{1/2}$ and $2p_{3/2}$ doublet peaks for titanium (Ti 2p) and oxygen (O 1s), respectively. From region quantification, we assess the atomic concentration ratio of potassium, oxygen, and titanium to correspond to ~1 : 6 : 2. This ratio indicates traces of potassium within the investigated sample, likely a residue component of the saturated KOH synthesis electrolyte during electrochemical erosion. Furthermore, the significant oxygen concentration implies that the nanowires are not composed of elemental titanium but rather consist of its oxidized form. Further analysis confirms the presence of various oxidation states of Ti within the material, primarily including Ti^{3+}, Ti^{4+}, and a neglectable amount of non-stoichiometric $Ti^{\delta+}$. For the Ti^{3+} and Ti^{4+} oxidation states of titanium, we quantified the respective ratio Ti^{3+} : Ti^{4+} to 1 : 16. From XPS results, we assume that our fabricated nanowires consist largely of titanium in a Ti^{4+} oxidation state, *i.e.*, a TiO_2-like composition, which is close to the non-stoichiometric Ti_9O_{17} compound determined by the TEM characterization.

Elemental composition of Ti_9O_{17} nanowires

In agreement with the XPS results, STEM imaging with a high-angle annular dark-field detector (STEM-HAADF) complemented with EDX elemental mapping identified titanium, oxygen, and potassium, as displayed in Fig. 3c–f. Quantification of the EDX spectra, summarized in Fig. S4 (ESI†), reveals a Ti : O ratio

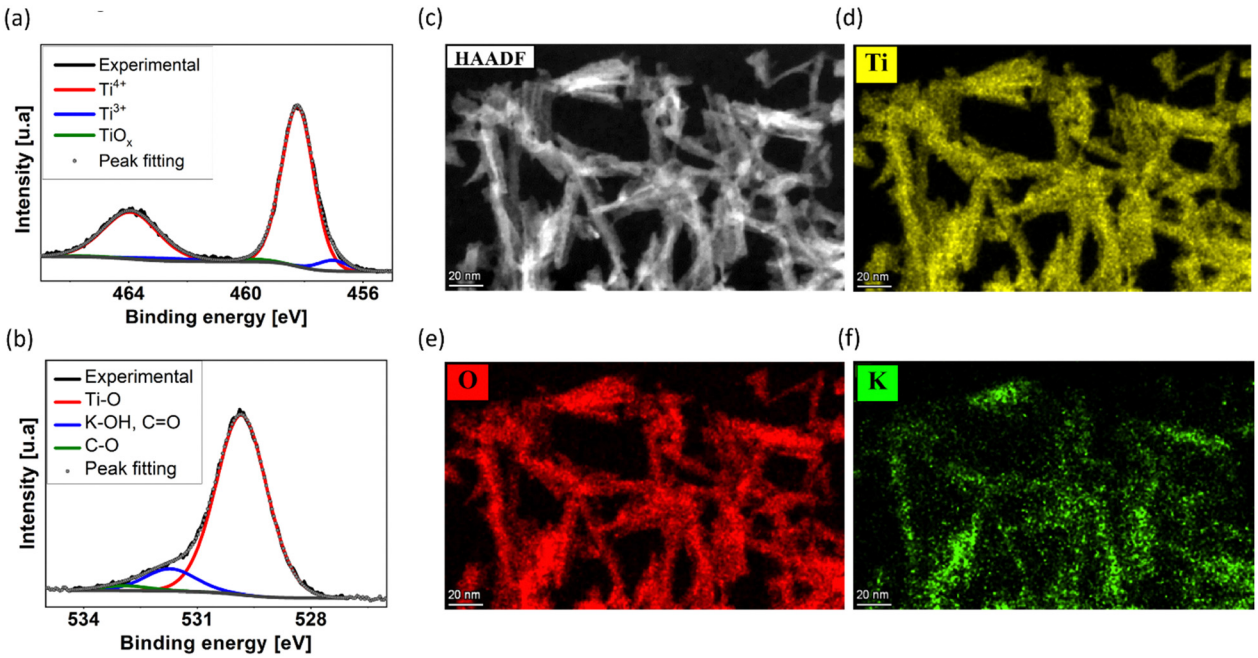

Fig. 3 (a) And (b) XPS spectra of the synthesized nanowires with the $2p_{1/2}$ and $2p_{3/2}$ doublet peaks for Ti 2p and O 1s, respectively. The peaks indicate the presence of Ti with different oxidation states. (c) STEM-HAADF image of a nanowire network. (d), (e) and (f) corresponding STEM-EDX elemental maps of nanowires for Ti–K, O–K, and K–K, respectively.

of 1 : 2, supporting the presence of a TiO_2-like structure of the nanowire network, *i.e.*, the oxidation state Ti^{4+}, as well as a small amount of potassium of about 3–5 at%. From XPS and EDX evaluation, we hypothesize the synthesis of ultrathin TiO_2-like nanowires by our simple, facile, and environmentally friendly methodology without any surfactants or additives, employing electrochemical erosion.

Diffraction experiments of Ti_9O_{17} nanowires

To gain more precise information about the structure of the nanowires, diffraction experiments in HR-XRD and PDF mode were performed, shown in Fig. 4a and b, respectively. The HR-XRD pattern can be modeled using a superposition of contributions from the non-stoichiometric compound Ti_9O_{17} and two side phases, namely $KTiO_2(OH)$ and metallic (hcp) titanium.[31,38] Both side phases have been found to exhibit coherent scattering lengths comparable with the resolution limit of the diffractometer (~100 nm), while an average crystallite size of 74 Å was determined for Ti_9O_{17}. This suggests a rather large crystal structure of the two side phases, which does not coincide with the ultrathin nanowires with a diameter of ~5 nm examined by the TEM characterization. Therefore, we assume metallic (hcp) titanium and $KTiO_2(OH)$ to be side products in the synthesized sample in low amounts, which could not be entirely avoided, despite extensive washing procedures after the synthesis. Fig. 4b displays the pair distribution function $G(r)$ obtained from the PDF mode for the synthesized nanowires. The damping of $G(r)$ at increased correlation distances r is primarily caused by the low momentum transfers $Q_{max\text{-}inst}$ and Q_{max} limits set, making the correlation length above the effective detection limit. The dashed vertical lines showcase the maximum peaks, and the small tickmarks illustrate the interatomic distances in the parent titanium oxides rutile, anatase, and TiO. From this, it is evident that Ti^{2+} cannot be found in the bulk, and the maximum peaks align rather well with the tickmarks of the parent anatase form of TiO_2. This confirms the presence of a TiO_2-like phase of our nanowires, or more accurately, a non-stoichiometric Magnéli phase Ti_9O_{17} structure according to HR-XRD, FFT, and SAED. Fig. S6 (ESI†) shows the difference in the crystal structure between rutile, anatase, and Ti_9O_{17}, which serves as the basis for the model used to describe the Ti_9O_{17} structure *via* HR-XRD. In addition, the small tail observed at ~2.85 Å can be identified as Ti–Ti or K–O distances most likely arising from $KTiO_2(OH)$ and metallic (hcp) titanium phases, in agreement with the conducted HR-XRD mode. Besides this, a weak correlation at $r \sim 1.45$ Å can indicate weak carbon contamination (C–C bond), which is always present when working under atmospheric conditions.

Elemental mapping of single Ti_9O_{17} nanowires

The results obtained from XRD and PDF average the structural information over many nanowires due to the large probing area. Nevertheless, in addition to the STEM-EDX, chemical analysis within the volume of single nanowires can be performed by using STEM-EELS measurements with higher sensitivity than the previously used EDX technique. Fig. 4a shows a single nanowire with the respective line-scan position where the chemical composition profile was measured. Furthermore, Fig. 5a illustrates elemental maps of potassium, oxygen, and titanium of the probed nanowire. Quantification of EEL spectra then provided percent composition (at%) profiles in Fig. 4b of the three elements across the nanowire shown in Fig. 4a. Remarkably, the atomic concentration profile indicates that the core of the nanowire contains ~3–4 at% of potassium, which is in agreement with STEM-EDX. Following the discussion of the XRD results, the sharp peaks in Fig. 4a correspond to relatively large $KTiO_2(OH)$ crystallites as only a small amount of potassium was detected *via* EELS in the core of the nanowires within dimensions of a few nm. Therefore, we exclude $KTiO_2(OH)$, found *via* XRD, as a potential candidate for the crystal structure of the nanowires and hypothesize the presence of Ti_9O_{17} nanowires. From the line-scan profile in Fig. 5b, we calculated an averaged Ti : O ratio of 0.63 ± 0.08, which

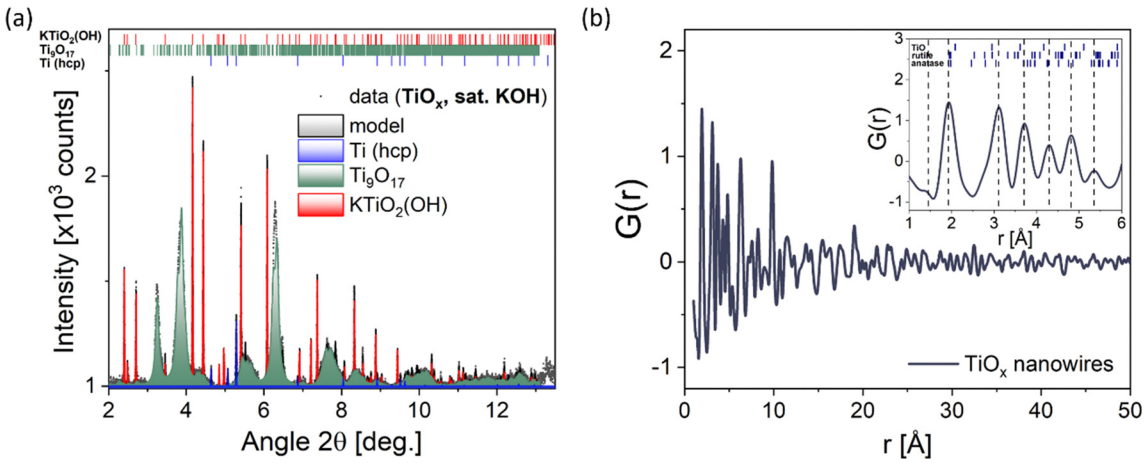

Fig. 4 (a) Background-subtracted, high-resolution XRD pattern of ultrathin nanowires synthesized in saturated KOH solution *via* the electrochemical top-down approach with modeling results. Contributions from different phases are displayed by color, and vertical tickmarks correspond to the calculated Bragg reflection positions. (b) Pair distribution function $G(r)$ determined from diffraction data in PDF mode. Dashed vertical lines correspond to the maximum peaks for the Ti_9O_{17} nanowires, and small tickmarks illustrate interatomic distances in parent TiO_2 rutile, anatase, and TiO.

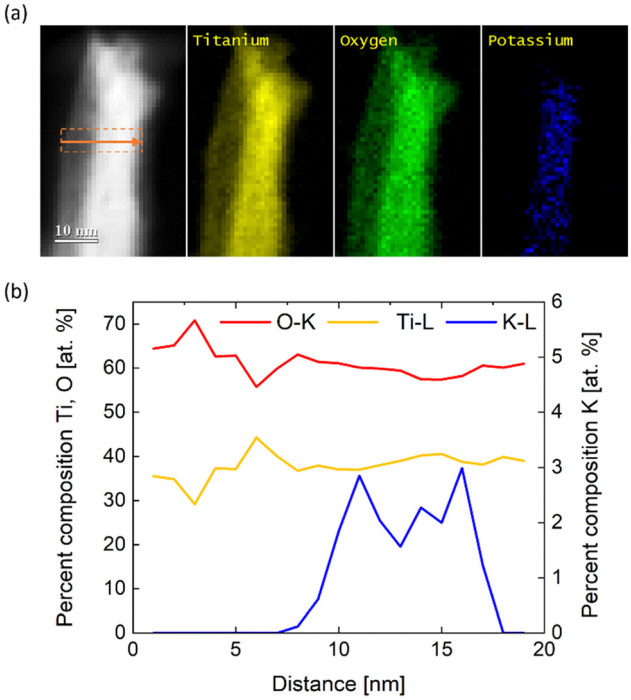

Fig. 5 STEM-EELS analysis of the chemical composition of single nanowires synthesized in saturated KOH. (a) HAADF-STEM image of a probed single nanowire and corresponding STEM-EELS elemental maps calculated from intensities of Ti–L, O–K, and K–L edges. (b) Chemical composition profile of the elements after quantification to atomic concentrations. The position of the profile is marked by the orange arrow in (a). The orange rectangle depicts the used integration width for each profile to denoise the data output.

approximates the expected Ti : O ratio of Ti_9O_{17} and thus confirms the presence of nanowires with Ti_9O_{17} crystal structure. Another interesting finding from EELS mapping is that potassium is present only in the core of the nanowires. It can indicate the beneficial role of synthesis in saturated KOH. K^+ dissolved in the saturated electrolyte could serve as a scaffold or seed for the growth of the nanowires. However, a more fundamental examination of the synthesis procedure needs to be conducted to prove these assumptions and reveal the origin of the formation of nanowires *via* electrochemical erosion.

Conclusions

In this work, we presented a novel top-down approach, called electrochemical erosion, to synthesize Magnéli phase Ti_9O_{17} nanowires as a versatile material with promising potential for future advancements in electronics and energy technologies. This simple and facile one-pot technique yields ultrathin nanowires with a diameter of ~5 nm and a large BET surface area of ~215 m^2 g^{-1}, comparable to state-of-the-art TiO_2 nanowires. Comparative measurements, including a range of analytical TEM techniques in combination with XPS and state-of-the-art HR-XRD and PDF characterizations, provided deep insights into the structure, morphology, and composition of ultrathin, isotropic nanowires with a non-stoichiometric crystal structure close to TiO_2, namely Ti_9O_{17}. These Magnéli phase nanowires could provide a promising opportunity to boost catalyst performance in (electro) catalysis as a stable, conductive, and high-surface area support material, which needs further investigation for particular applications. Furthermore, STEM-EELS measurements revealed not only a TiO_2-like chemical composition of single nanowires but also revealed that the core of nanowires seems to contain a small amount of potassium. This could stem from the electrolyte used during the synthesis and could be crucial for the formation of nanowires. However, further in-depth investigation is necessary to determine the role of potassium in the synthesis of Ti_9O_{17} nanowires. We want to highlight the great advantage of our synthesis approach, *i.e.*, we can prevent environmental and health concerns by avoiding harmful precursor solutions or surfactants and eliminating complex, multi-step synthesis routes containing high-temperature profiles compared to conventional synthesis techniques. It is important to note again that standard health and safety precautions have to be obeyed when handling nanostructured materials, such as Ti_9O_{17} nanowires, due to their nano-size-related toxicity in order to guarantee the fabrication and application of these novel materials.

Conflicts of interest

There are no conflicts to declare.

Acknowledgements

We want to thank Siegfried Schreier, Kathrin L. Kollmannsberger, Shujin Hou for their help with the conducted SEM and BET experiments, respectively. P. M. S. and A. S. B. are thankful for the funding *via* the Excellence Strategy of the Federal Government and the Länder in the context of the ARTEMIS Innovation Network and DFG project BA 5795/6-1. The authors are grateful for the funding support by the DFG Cluster of Excellence "e-conversion". The authors acknowledge support from the Ministry of Education, Youth and Sports of the Czech Republic for supporting Large Research Infrastructures CEMNAT (LM2023037) and CzechNanoLab (LM2023051) for providing SEM, XRD, XPS and TEM accesses, respectively.

References

1 S. Liang, X. Wang, R. Qi, Y.-J. Cheng, Y. Xia, P. Müller-Buschbaum and X. Hu, *Adv. Funct. Mater.*, 2022, **32**, 2201675; H. Shi, C. Shi, Z. Jia, L. Zhang, H. Wang and J. Chen, *RSC Adv.*, 2022, **12**, 33641; S. Liang, X. Wang, Y. J. Cheng, Y. Xia and P. Müller-Buschbaum, *Energy Storage Mater.*, 2022, **45**, 201–264.

2 Q. Wang, Z. H. Wen and J. H. Li, *Adv. Funct. Mater.*, 2006, **16**, 2141–2146; X. Lu, M. Yu, G. Wang, T. Zhai, S. Xie, Y. Ling, Y. Tong and Y. Li, *Adv. Mater.*, 2013, **25**, 267–272; S. Yang, Y. Lin, X. Song, P. Zhang and L. Gao, *ACS Appl. Mater. Interfaces*, 2015, **7**, 17884–17892; P. Pazhamalai,

K. Krishnamoorthy, V. K. Mariappan and S.-J. Kim, *J. Colloid Interface Sci.*, 2019, **536**, 2–70; W. Zhong, H. Sun, J. Pan, Y. Zhang, X. Yan, Y. Guan, W. Shen and X. Cheng, *Mater. Sci. Semicond. Process.*, 2021, **127**, 105715.

3 J. Bai and B. Zhou, *Chem. Rev.*, 2014, **114**, 10131–10176; X. Tian, X. Cui, T. Lai, J. Ren, Z. Yang, M. Xiao, B. Wang, X. Xiao and Y. Wang, *Nano Mater. Sci.*, 2021, **3**, 390–403; B. B. Azer, A. Gulsaran, J. R. Pennings, R. Saritas, S. Kocer, J. L. Bennett, Y. D. Abhang, M. A. Pope, E. Abdel-Rahman and M. Yavuz, *J. Electroanal. Chem.*, 2022, **918**, 116466; L. Bertel, D. A. Miranda and J. M. García-Martín, *Sensors*, 2021, **21**, 6167; S. Jafari, B. Mahyad, H. Hashemzadeh, S. Janfaza, T. Gholikhani and L. Tayebi, *Int. J. Nanomed.*, 2020, **15**, 3447–3470.

4 A. Fujishima, T. N. Rao and D. A. Tryk, *J. Photochem. Photobiol., C*, 2000, **1**, 1–21; M. Ni, M. K. H. Leung, D. Y. C. Leung and K. Sumathy, *Renewable Sustainable Energy Rev.*, 2007, **11**, 401–425; M. Pelaez, N. T. Nolan, S. C. Pillai, M. K. Seery, P. Falaras, A. G. Kontos, P. S. M. Dunlop, J. W. J. Hamilton, J. A. Byrne, K. O'Shea, M. H. Entezari and D. D. Dionysiou, *Appl. Catal., B*, 2012, **125**, 331–349; X. Kang, S. Liu, Z. Dai, Y. He, X. Song and Z. Tan, *Catalysts*, 2019, **9**, 191; M. Ijaz and M. Zafar, *Int. J. Energy Res.*, 2021, **45**, 3569–3589.

5 A. Fujishima and K. Honda, *Nature*, 1972, **238**, 37–38.

6 M. Pudukudy, Q. Jia, J. Yuan, S. Megala, R. Rajendran and S. Shan, *Mater. Sci. Semicond. Process.*, 2020, **108**, 104891; J. Yuan, M. Pudukudy, T. Hu, Y. Liu, X. Luo, Y. Zhi, H. Su, L. Jiang and S. Shan, *Appl. Surf. Sci.*, 2021, **557**, 149829.

7 Z. Kang, G. Yang, J. Mo, S. Yu, D. A. Cullen, S. T. Retterer, T. J. Toops, M. P. Brady, G. Bender, B. S. Pivovar, J. B. Green Jr. and F.-Y. Zhang, *Int. J. Hydrogen Energy*, 2018, **43**, 14618–14628; M. F. Ernst, V. Meier, M. Kornherr and H. A. Gasteiger, *Meet. Abstr.*, 2022, MA2022-01 1750.

8 L. K. Noda, R. M. de Almeida, L. F. D. Probst and N. S. Gonçalves, *J. Mol. Catal. A: Chem.*, 2005, **225**, 39–46; H. Zhao, P. Jiang, Y. Dong, M. Huang and B. Liu, *New J. Chem.*, 2014, **38**, 4541–4548; J. Gardy, A. Hassanpour, X. Lai and M. H. Ahmed, *Appl. Catal., A*, 2016, **527**, 81–95.

9 S. D. Lin, M. Bollinger and M. A. Vannice, *Catal. Lett.*, 1993, **17**, 245–262; V. Idakiev, Z.-Y. Yuan, T. Tabakova and B.-L. Su, *Appl. Catal., A*, 2005, **281**, 149–155; K.-W. Park and K.-S. Seol, *Electrochem. Commun.*, 2007, **9**, 2256–2260; B. Dong, B.-L. He, J. Huang, G.-Y. Gao, Z. Yang and H.-L. Li, *J. Power Sources*, 2008, **175**, 266–271; M. Méndez-Cruz, J. Ramírez-Solís and R. Zanella, *Catal. Today*, 2011, **166**, 172–179; R. Palcheva, L. Dimitrov, G. Tyuliev, A. Spojakina and K. Jiratova, *Appl. Surf. Sci.*, 2013, **165**, 309–316; X.-L. Sui, Z.-B. Wang, M. Yang, L. Huo, D.-M. Gu and G.-P. Yin, *J. Power Sources*, 2014, **255**, 43–51; A.-R. Rautio, P. Mäki-Arvela, A. Aho, K. Eränen and K. Kordas, *Catal. Today*, 2015, **241**, 170–178; S. K. S. Hossain, J. Saleem, S. Rahman, S. M. J. Zaidi, G. McKay and C. K. Cheng, *Catalysts*, 2019, **9**, 298; H. A. Lara-García, J. A. Mendoza-Nieto, H. Pfeiffer and L. Torrente-Murciano, *Int. J. Hydrogen Energy*, 2019, **44**, 30062–30074; S. Hoang, Y. Guo, A. J. Binder, W. Tang, S. Wang, J. Liu, H. Tran, X. Lu, Y. Wang, Y. Ding, E. A. Kyriakidou, J. Yang, T. J. Toops, T. R. Pauly, R. Ramprasad and P.-X. Gao, *Nat. Commun.*, 2020, **11**, 1062; T. Fröschl, U. Hörmann, P. Kubiak, G. Kučerová, M. Pfanzelt, C. K. Weiss, R. J. Behm, N. Hüsing, U. Kaiser, K. Landfester and M. Wohlfahrt-Mehrens, *Chem. Soc. Rev.*, 2012, **41**, 5313–5360; S. Bagheri, N. M. Julkapli and S. B. A. Hamid, *Sci. World J.*, 2014, 727496.

10 M. Pudukudy, Z. Yaakob, A. Kadier, M. S. Takriff and N. S. M. Hassan, *Int. J. Hydrogen Energy*, 2017, **42**, 16495–16513.

11 A. Walcarius, *Chem. Soc. Rev.*, 2013, **42**, 4098–4140.

12 S. Ghosh, T. Maiyalagan and R. N. Basu, *Nanoscale*, 2016, **8**, 6921–6947.

13 E. Auer, A. Freund, J. Pietsch and T. Tacke, *Appl. Catal., A*, 1998, **173**, 259–271.

14 Z. Zhang, J. Liu, J. Gu, L. Su and L. Cheng, *Energy Environ. Sci.*, 2014, **7**, 2535–2558.

15 S. J. Tauster, S. C. Fung, R. T. K. Baker and J. A. Horsley, *Science*, 1981, **211**, 1121–1125; X. Du, Y. Huang, X. Pan, B. Han, Y. Su, Q. Jiang, M. Li, H. Tang, G. Li and B. Qiao, *Nat. Commun.*, 2020, **11**, 5811.

16 L. Dai, C. H. Sow, C. T. Lim, W. C. D. Cheong and V. B. C. Tan, *Nano Lett.*, 2009, **9**, 576–582; P. Roy, S. Berger and P. Schmuki, *Angew. Chem., Int. Ed.*, 2011, **50**, 2904–2939; Y. Takabatake, Z. Noda, S. M. Lyth, A. Hayashi and K. Sasaki, *Int. J. Hydrogen Energy*, 2014, **39**, 5074–5082.

17 J. Thakare and J. Masud, *Energies*, 2022, **15**, 4437.

18 S. Sharifi, S. Behzadi, S. Laurent, M. L. Forrest, P. Stroeve and M. Mahmoudi, *Chem. Soc. Rev.*, 2012, **41**, 2323–2343; P. Ganguly, A. Breen and S. C. Pillai, *ACS Biomater. Sci. Eng.*, 2018, **4**, 2237–2275; M. Allegri, M. G. Bianchi, M. Chiu, J. Varet, A. L. Costa, S. Ortelli, M. Blosi, O. Bussolati, C. A. Poland and E. Bergamaschi, *PLoS One*, 2016, **11**, e0151365.

19 A. F. Arif, R. Balgis, T. Ogi, F. Iskandar, A. Kinoshita, K. Nakamura and K. Okuyama, *Sci. Rep.*, 2017, **7**, 3646; Y. Fan, X. Feng, W. Zhou, S. Murakami, K. Kikuchi, N. Nomura, L. Wang, W. Jiang and A. Kawasaki, *J. Eur. Ceram. Soc.*, 2018, **38**, 507–513.

20 A. A. Gusev, E. G. Avvakumov, A. Zh. Medvedev and A. I. Masily, *Sci. Sintering*, 2007, **39**, 51–57.

21 W.-Q. Han and X.-L. Wang, *Appl. Phys. Lett.*, 2010, **97**, 243104; X. Li, A. L. Zhu, W. Qu, H. Wang, R. Hui, L. Zhang and J. Zhang, *Electrochim. Acta*, 2010, **55**, 5891–5898; H. Zhao, Y. Wang, Q. Tang, L. Wang, H. Zhang, C. Quan and T. Qi, *Int. J. Hydrogen Energy*, 2014, **39**, 9621–9627.

22 S. T. Nguyen, J.-M. Lee, Y. Yang and X. Wang, *Ind. Eng. Chem. Res.*, 2012, **51**, 9966–9972.

23 H. Zhao, Y. Wang, Q. Tang, L. Wang, H. Zhang, C. Quan and T. Qi, *Int. J. Hydrogen Energy*, 2014, **39**, 9621–9627.

24 Q. He, Q. Hao, G. Chen, B. Poudel, X. Wang, D. Wang and Z. Ren, *Appl. Phys. Lett.*, 2007, **91**, 052505; M. Backhaus-Ricoult, J. R. Rustad, D. Vargheese, I. Dutta and K. Work, *J. Electron. Mater.*, 2012, **41**, 1636–1647; Y. Fan, X. Feng,W.

Zhou, S. Murakami, K. Kikuchi, N. Nomura, L. Wang, W. Jiang and A. Kawasaki, *J. Eur. Ceram. Soc.*, 2018, **38**, 507–513.

25 X. Chen and S. S. Mao, *Chem. Rev.*, 2007, **107**, 2891–2959; X. Wang, Z. Li, J. Shi and Y. Yu, *Chem. Rev.*, 2014, **114**, 9346–9384; Y. Wang, Y. He, Q. Lai and M. Fan, *J. Environ. Sci.*, 2014, **26**, 2139–2177; X. Chen and S. S. Mao, *J. Nanosci. Nanotechnol.*, 2006, **6**, 906–925; S. Reghunat, D. Pinherio and S. D. Kr, *Appl. Surf. Sci. Adv.*, 2021, **3**, 100063; M. Ge, C. Cao, J. Huang, S. Li, Z. Chen, K.-Q. Zhang, S. S. Al-Deyab and Y. Lai, *J. Mater. Chem. A*, 2016, **4**, 6772–6801; B. Xu, H. Y. Sohn, Y. Mohassab and Y. Lan, *RSC Adv.*, 2016, **6**, 79706–79722; X. Zhang, Y. Lin, X. Zhong, L. Wang, W. Liu, A. Singh and Q. Zhao, *J. Mater. Sci: Mater. Electron.*, 2016, **27**, 4861–4865; S. Qian and J. Mao, *J. Mater. Sci: Mater. Electron.*, 2015, **26**, 5166–5169.

26 J. Joo, S. G. Kwon, T. Yu, M. Cho, J. Lee, J. Yoon and T. Hyeon, *J. Phys Chem. B*, 2005, **109**, 15297–15302; P. D. Cozzoli, A. Kornowski and H. Weller, *J. Am. Chem. Soc.*, 2003, **125**, 14539–14548; Y.-W. Jun, M. F. Casula, J.-H. Sim, S. Y. Kim, J. Cheon and A. P. Alivisatos, *J. Am. Chem. Soc.*, 2003, **125**, 15981–15985; X.-L. Li, Q. Peng, J.-X. Yi, X. Wang and Y. Li, *Chem. – Eur. J.*, 2006, **12**, 2383–2391; J. Hu, H. Li, S. Muhammad, Q. Wu, Y. Zaho and Q. Jiao, *J. Solid State Chem.*, 2017, **253**, 113–120.

27 S. O. Badmus, H. K. Amusa, T. A. Oyehan and T. A. Saleh, *Environ. Sci. Pollut. Res.*, 2021, **28**, 62085–62104; S. Rebello, A. K. Asok, S. Mundayoor and M. S. Jisha, *Environ. Chem. Lett.*, 2014, **12**, 275–287; M. Lechuga, M. Fernández-Serrano, E. Jurado, J. Núñez-Olea and F. Ríos, *Ecotoxicol. Environ. Saf.*, 2016, **125**, 1–8.

28 G. Bredig and F. Haber, *Ber. Dtsch. Chem. Ges.*, 1898, **31**, 2741–2752.

29 X. Chen, S. Chen, W. Huang, J. Zheng and Z. Li, *Electrochim. Acta*, 2009, **54**, 7370–7373; W. Huang, S. Chen, J. Zheng and Z. Li, *Electrochem. Commun.*, 2009, **11**, 469–472; J. Liu, W. Huang, S. Chen, S. Hu, F. Liu and Z. Li, *Int. J. Electrochem. Sci.*, 2009, **4**, 1302–1308; A. I. Yanson, P. Rodriguez, N. Garcia-Araez, R. V. Mom, F. D. Tichelaar and M. T. M. Koper, *Angew. Chem.*, 2011, **123**, 6470–6474; T. J. P. Hersbach, I. T. McCrum, D. Anastasiadou, R. Wever, F. Calle-Vallejo and M. T. M. Koper, *ACS Appl. Mater. Interfaces*, 2018, **10**, 39363–39379; A. I. Yanson, P. V. Antonov, P. Rodriguez and M. T. M. Koper, *Electrochim. Acta*, 2013, **112**, 913–918; P. Rodriguez, F. D. Tichelaar, M. T. M. Koper and A. I. Yanson, *J. Am. Chem. Soc.*, 2011, **133**, 17626–17629.

30 J. Fichtner, B. Garlyyev, S. Watzele, H. A. El-Sayed, J. N. Schwämmlein, W.-J. Li, F. Maillard, L. Dubau, J. Michalička, J. M. Macak, A. Holleitner and A. S. Bandarenka, *ACS Appl. Mater. Interfaces*, 2019, **11**, 5129–5135; B. Garlyyev, S. Watzele, J. Fichtner, J. Michalička, A. Schökel, A. Senyshyn, A. Perego, D. Pan, H. A. El-Sayed, J. M. Macak, P. Atanassov, I. V. Zenyuk and A. S. Bandarenka, *Nano Res.*, 2021, **14**, 2762–2769.

31 P. J. Thomas and R. D. Twesten, *Microsc. Microanal.*, 2012, **18**, 968–969.

32 A.-C. Dippel, H.-P. Liermann, J. T. Delitz, P. Walter, H. Schulte-Schrepping, O. H. Seeck and H. Franz, *J. Synchrotron Radiat.*, 2015, **22**, 675–687.

33 A. P. Hammersley, S. O. Svensson, M. Hanfland, A. N. Fitch and D. Hausermann, *High Press. Res.*, 1996, **14**, 235–248.

34 J. Rodríguez-Carvajal, Commission on Powder Diffraction (IUCr), *Newsletter*, 2001, **26**, 12–19.

35 P. Juhás, T. Davis, C. L. Farrow and S. J. L. Billinge, *J. Appl. Cryst.*, 2013, **46**, 560–566.

36 S. Çetinkaya, G. Khamidov, L. Özcan, L. Palmisano and S. Yurdakal, *Front. Chem.*, 2022, 10; J.-S. Lee, Y.-I. Lee, H. Song, D.-H. Jang and Y.-H. Choa, *Curr. Appl. Phys.*, 2011, **11**, S210–S214; Y. Meng, D. Wang, Y. Zhao, R. Lian, Y. Wei, X. Bian, Y. Gao, F. Du, B. Liu and G. Chen, *Nanoscale*, 2017, **9**, 12934–12940; Z. P. Tshabalala, T. P. Mokoena, M. Jozela, J. Tshilongo, T. K. Hillie, H. C. Swart and D. E. Motaung, *ACS Appl. Nano Mater.*, 2021, **4**, 702–716; H. B. Wu, H. H. Hng and X. W. Lou, *Adv. Mater.*, 2012, **24**, 2567–2571.

37 S. Andersson and L. Jahnberg, *Mater. Sci.*, 1963, **21**, 413–426.

38 N. Masaki, S. Uchida, H. Yamane and T. Sato, *Chem. Mater.*, 2002, **14**, 419–424.